Int. J. Radiation Oncology Biol. Phys., Vol. 66, No. 4, pp. 1263–1270, 2006

0360-3016/06/$–see front matter

ELSEVIER

doi:10.1016/j.ijrobp.2006.07.1363

PHYSICS CONTRIBUTION

FEASIBILITY OF FULLY AUTOMATED DETECTION OF FIDUCIAL MARKERS IMPLANTED INTO THE PROSTATE USING ELECTRONIC PORTAL IMAGING: A COMPARISON OF METHODS

EMMA J. HARRIS, PH.D.,* HELEN A. MCNAIR, M.SC.,† AND PHILLIP M. EVANS, PH.D.*

*Joint Department of Physics, Institute of Cancer Research, Sutton, Surrey, United Kingdom; †Department of Radiotherapy, The Royal Marsden NHS Foundation Trust, Sutton, Surrey, United Kingdom

Purpose: To investigate the feasibility of fully automated detection of fiducial markers implanted into the prostate using portal images acquired with an electronic portal imaging device.

Methods and Materials: We have made a direct comparison of 4 different methods (2 template matching-based methods, a method incorporating attenuation and constellation analyses and a cross correlation method) that have been published in the literature for the automatic detection of fiducial markers. The cross-correlation technique requires a-priory information from the portal images, therefore the technique is not fully automated for the first treatment fraction. Images of 7 patients implanted with gold fiducial markers (8 mm in length and 1 mm in diameter) were acquired before treatment (set-up images) and during treatment (movie images) using 1MU and 15MU per image respectively. Images included: 75 anterior (AP) and 69 lateral (LAT) set-up images and 51 AP and 83 LAT movie images. Using the different methods described in the literature, marker positions were automatically identified.

Results: The method based upon cross correlation techniques gave the highest percentage detection success rate of 99% (AP) and 83% (LAT) set-up (1MU) images. The methods gave detection success rates of less than 91% (AP) and 42% (LAT) set-up images. The amount of a-priory information used and how it affects the way the techniques are implemented, is discussed.

Conclusions: Fully automated marker detection in set-up images for the first treatment fraction is unachievable using these methods and that using cross-correlation is the best technique for automatic detection on subsequent radiotherapy treatment fractions. © 2006 Elsevier Inc.

Fiducial marker, Radiotherapy, Motion, Automatic detection, Electronic portal imaging.

INTRODUCTION

Variations in patient position and tumor movement will lead to errors in the targeting of dose to the tumor in conformal radiotherapy. In general, to reduce the effects of errors in patient set-up and day-to-day variations of the average tumor position (interfraction motion), position verification is performed using electronic portal imaging devices (EPIDs) before treatment. Because the prostate cannot easily be visualized with megavoltage portal imaging, conventionally, for prostate radiotherapy patients, position set-up errors have been determined by matching the position of the bony anatomy in the portal image to that in digitally reconstructed radiographs (DRRs). However, because the position of the prostate does not necessarily remain fixed with respect to the position of the pelvis, the use of fiducial markers implanted into the prostate is increasing (1). Made from high-density and high atomic number material, such as gold, markers are more radio-opaque than soft tissue and provide greater image contrast and therefore they are more visible in portal images. The 3D position coordinates of each marker can be found from 2 portal images acquired at 2 different angles. By using the coordinates of the center of mass of 3 or more fiducial markers, the position of the prostate can be more accurately identified. However, in lateral views, markers are often not clearly visible, due to the presence of highly attenuating patient anatomy such as the femoral heads and the pelvis. In this case, a-priory knowledge of the marker position at the time of the planning CT can assist and commonly this is in the form of the DRRs in which markers are more readily visualized. Automatic detection of fiducial markers will simplify marker identification; removing the need for operators to manually "match" the portal image to the DRR and therefore speed up the position verification process. Tumor movement

Reprint requests to: Emma J. Harris, Ph.D., Institute of Cancer Research, Joint Department of Physics, Cotswold Road, Sutton, Surrey, SM2 5PT, United Kingdom. Tel: (+44) 208-6613478; Fax: (+44) 208-6433812; E-mail: eharris@icr.ac.uk

Acknowledgments—The authors acknowledge Vibeke N. Hansen for her useful discussions and Cancer Research-UK for funding this work under Programme Grant Reference No. C46/A3970.

Received March 10, 2006, and in revised form July 19, 2006. Accepted for publication July 19, 2006.

during treatment (intrafraction motion) is another potential source of error in dose delivery. Intrafractional prostate gland motion has been assessed by various groups. Ghilezan *et al.* (2), in one of the most recent publications regarding this topic, observe intrafraction motion using magnetic resonance imaging, but also review the work of other authors who have measured intrafraction prostate motion using various techniques. Ghilezan *et al.* find that the most significant motion (>3 mm up to 10 mm) is due to rectal filling and gas, in line with the conclusions of the articles they review.

If the treatment beam's dimensions are such that all markers can be visualized in the beams-eye-view throughout the treatment then portal images acquired continuously during treatment can also be used to monitor target position. Also, markers can also be imaged using fluoroscopy acquired with on-board kV imagers. Combining the information from portal imaging and from an on-board imager placed orthogonal to the EPID will provide marker positions in 3D. This could potentially enable the treatment to be "gated" i.e., the treatment can be stopped when the markers move out of a predetermined treatment space. This approach is not suited to treatments which require small segments or complex dynamic delivery as the markers need to be visualized in the beams-eye-view, i.e., in the portal image. An alternative method for the measurement of marker positions in 3D is using 2 kV imagers. Shimizu *et al.* (3) have pioneered this approach using 2 fluoroscopy units that acquire images during treatment. All of these approaches to intrafraction motion monitoring require a method to determine the position of the markers in real-time and therefore will also require an automatic detection algorithm to quickly find the position of the makers in the image and hence facilitate fast marker location feedback to the gating system.

There are a large number of image processing techniques to find objects within an image for a large range of applications (4). A number of authors have presented different methods for the automatic detection of markers implanted in the prostate, using EPIDs. We have chosen to concentrate on these as they have directly applied their image processing techniques to clinical images. Balter *et al.* (5) in 1995 were the first group to address the technical feasibility of automated localization of the prostate. Using a reference image acquired on the first day of treatment, Balter *et al.* demonstrated the automatic detection of markers implanted in both humanoid phantom and patients. Nederveen *et al.* (6, 7), in 2000 and 2001, measured detection success rates and localization accuracy using an automatic detection algorithm based upon a rectangular Marker Extraction Kernel (MEK) specifically designed to mimic the appearance of cylindrical fiducial markers. A similar approach was adopted in 2003 by Buck *et al.* (8), who used a Mexican hat filter (MHF) to identify spherical markers. Also in 2003, Aubin *et al.* (9) described an automatic detection algorithm that first uses a series of image processing techniques to enhance portal images and then identify marker locations that are initially determined from points of local minimum intensity (corresponding to maximum X-ray attenuation). Locations are verified through the application of image filters or templates and then by constellation analysis that uses the spatial relationship between markers. Table 1 summarizes the study parameters for each of the published studies. The greater challenge for portal imaging is the lateral (LAT) views and therefore percentage detection success rates published by the authors for lateral views are presented in Table 1 (with the exception of Buck *et al.,* who considered anterior-posterior (AP) views only). Direct comparison of these methods and their reported detection success rates is problematic due to variation of the study parameters. For example, Nederveen *et al.* report 99% detection rate for 1.2 mm diameter markers, however markers were not inserted into the prostate but placed on the patients skin at beam exit. Due to X-ray imaging geometry, placing the markers at beam exit (closer to the EPID) will make them appear smaller in the image and therefore arguably more difficult to detect than those positioned inside the prostate. However, by placing the markers at the skin exit, they will attenuate scatter from the patient and the markers will have greater image contrast, which improves the probability of detection. Clearly making a comparison of detection efficiencies for markers placed at different positions is

Table 1. Summary of study parameters and detection efficiencies for the four different methods of automatic detection of fiducial markers implanted into the prostate that were compared

	Balter (1995)	Nederveen (2001)	Buck (2003)	Aubin (2003)
Marker size	1.6 mm ∅ sphere (Au)	1.0 mm∅ × 5 mm (Au) 1.2 mm∅ × 5 mm (Au) 1.0 mm∅ × 10 mm (Au)	1.0 mm ∅ sphere (W) 1.5 mm ∅ sphere (W) 2.0 mm ∅ sphere (W)	1.6 mm∅ × 2.6 mm (Au)
Marker location	Prostate	Skin (beam exit)	Skin (beam entry)	Prostate
Total no. patients/Total no. lateral images in study	2/18	15/300	12/0	7/308
EPID	Theraview camera	Heimann a-Si flat panel	IView^{GT} a-Si flat panel	BeamView^{Plus} camera
Exposure (MU)	4 (6MV) 15 (15MV)	1.5 (18MV) open	3–5 (15MV)	75
Detection success rate %	88 (LAT)	99 (LAT) 90 (LAT) 95 (LAT)	0 (AP) 95 (AP) 99 (AP)	80 (LAT)

Abbreviations: EPID = electronic portal imaging device; LAT = lateral; MU = monitor units; MV = megavolts.

not straightforward. Similarly for the methods of Aubin and Balter, who employ markers that are close in size, comparison is difficult as they use different EPIDs and different numbers of monitor units (MUs).

In this article we make a direct comparison of the techniques described above by implementing each method for the detection of markers in portal images acquired of prostate patients that have had fiducial markers implanted into the prostate. For patient set-up it is prudent to use the automatic method to perform marker detection and then have these positions checked by a therapist. If the therapist observes that the marker was not detected correctly, they would have to intervene. Consequently, the higher the detection efficiency of the automated method, the less user intervention will be required. For intrafraction motion monitoring, user intervention is not possible as a fast update of marker position during treatment is required. In this case, the higher the detection efficiency the greater the percentage of treatment time we can be confident of the marker positions. By performing the marker detection on the same images we have determined which method gives the highest detection success rates for our images, enabling a direct comparison. In addition, we compare detection success rates for lower MU, set-up portal images and treatment time images. Each of these techniques requires some level of a-priory knowledge obtained either at the time of planning or from the portal images themselves. The amount of a-priory information used and how it effects the way the techniques are implemented, is discussed.

METHODS AND MATERIALS

Image acquisition

Before planning CT and treatment simulation 7 consenting patients had 3 gold markers implanted into their prostate under transrectal ultrasound guidance. These patients were part of an initial study (approved by local Research Ethics Committee) designed to assess the efficacy of fiducial markers for the assistance of patient position verification and the measurement of interfractional and intrafractional prostate motion. Markers are 8 mm in length and have a 1 mm diameter. A marker diameter of 1 mm can be inserted using the standard biopsy needle used for prostate biopsy and was chosen to minimize patient discomfort while the length of 8 mm was chosen to increase marker visibility. Both gold markers and bony anatomy were outlined on DRRs at the time of treatment planning. Portal set-up images were acquired before treatment on the first 5 days of treatment and once a week thereafter. Set-up images were acquired for each field using 1MU, 6MV and the field size was selected to include the bony anatomy for matching. Both AP and lateral projections were acquired. The treatment linac was an Elekta SLi, (Elekta Oncology Systems, Crawley, UK). In addition to set up images, a series of "movie" images were also acquired during treatment. Patients receive standard 3 field prostate treatment which uses large fields shaped with multi-leaf collimators therefore all 3 markers can be visualized using the treatment beam. One movie image is acquired in 2.28 s, this corresponds to approximately 15MU for a 400MU/min treatment dose rate. All images were acquired with an a-Si EPID (*iview*^{GT}). Patients are treated in the supine position and therefore we do not expect any movement of the markers due to respiratory motion (2). For this study, the image sets including the DRRs from 7 patients were used and included: 75 AP and 69 LAT set-up images and 51 AP and 83 LAT movie images. Lateral movie images obtained during treatment included an Eleketa motorized wedge. Treatment-time images acquired for 2 of the 7 patients contained greater than 3 mm marker movement. A typical LAT portal image is shown in Fig. 1a.

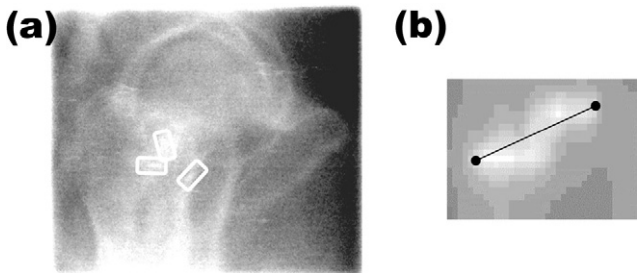

Fig. 1. (a) Lateral portal image of a patient with 3 fiducial markers implanted into the prostate. White boxes indicate the position of the fiducial markers that can be hard to visualize in the lateral images due to overlying bony anatomy. (b) Example region of digitally reconstructed radiograph image containing a fiducial marker. The length and orientation of the marker are calculated from the pixel coordinates of the ends of the marker that are identified manually.

Marker detection

The different marker detection methods that were compared are described in the literature (5–9). Each of the methods has been implemented following these descriptions, however to make greater use of the a-priory knowledge available and to make a fairer comparison of the techniques some steps have been added. These changes, and for completeness, brief descriptions of the methods, are given below.

A-priory knowledge. A-priory knowledge about the markers can be used to improve the accuracy and speed of the detection methods. For this study, this knowledge was obtained from the DRRs generated at the time of treatment planning and includes:

position with respect to the isocenter
length;
width;
orientation;
and inter-marker distances.

All values are projected to the imaging plane. Marker dimensions were found by identifying the co-ordinates of the ends of the marker. Using these co-ordinates the length and orientation of the markers were calculated (in pixel units relative to the isocenter). The pixel resolution of the DRRs differed and was dependant upon the field of view that had been chosen by the radiotherapy treatment planner. In general the pixel resolution also differed to that of the portal images and therefore these co-ordinates had to be re-scaled using the ratio of the pixel/mm in the DRR to that of the portal image which was 4.03 pixels/mm at the plane of the isocenter. The DRR pixel resolution was calculated using a fixed scale generated by the treatment planning system (Pinnacle treatment planning system, Philips) visible in the image. As an example part of a DRR marker image is shown in Figure 1b in which the ends of the marker are marked. Due to a small positional uncer-

tainty on the portal imager, which includes the effect of detector sag, the projection of the isocenter did not always coincide with the center of the portal imager. The projection of the isocenter was identified by finding the field edges using a maximum gradient technique (10) and using these as a reference to calculate its position. The position with respect to the isocenter, size and orientation of the markers as they would appear in the portal image could then be predicted. The width of the marker in the portal image was set to 4 pixel units which represents marker width of ~ 1 mm.

Cross-correlation (Balter method). Normalized cross-correlation can be used to find the similarity between 2 images (4). This method requires the greatest level of a-priory knowledge in that it uses a reference image of the marker selected from a portal image to carry out the search. Balter *et al.* (5) proposed using portal images obtained on the first day of treatment to create marker reference images that can then be cross-correlated with images obtained on subsequent treatment days. To implement this method, marker positions were manually identified from treatment time portal images acquired on the first day of treatment. Marker reference images used for the search were then obtained by selecting a region of interest around the marker location. Search areas of 64 × 64 pixels centered on predicted marker locations obtained using the DRR were defined. Projected to the plane of the isocenter, 64 pixels is equivalent to approximately 16 mm, which is twice the maximum distance that the prostate will move. This distance was employed by Balter *et al.* and has been kept constant for all of the methods. A uniform 2 × 2 averaging filter was applied to the reference image and the portal image to remove high frequency noise. A normalized cross-correlation was then performed for each marker at each pixel position within the search area by calculating the correlation coefficient (CC) (4). This produces an array of CCs the size of the search region. The CC is normalized to the average image intensity and ranges between 1 and −1, the closer to zero the CC is, the less similar the images. The marker position corresponds to the pixel with the highest absolute correlation coefficient.

Template matching (Nederveen and Buck methods). Both of the techniques described by Nederveen and Buck are based on template matching image processing techniques (4). Marker locations can be found by convolving the portal image with a digitally constructed template that has been chosen to mimic the projection of the fiducial marker. The image coordinates of the pixel with highest intensity in the resultant image corresponds to the marker position. Nederveen *et al.* (6) have presented a marker extraction kernel (MEK) to be used as a template. This template is illustrated in Fig. 2 and is represented by 3 rectangular regions, L_{ab}, L_ε and L_δ. The region dimensions (in pixels) are given by parameters a, b, ε and δ.

Because markers are cylindrical their rotational asymmetry means that marker projections will have varying width, length and orientation. For this study parameters a and b were found for each marker in both LAT and AP views using the DRRs. Parameters ε and δ were kept constant and equal to unity. Each region of the MEK is weighted using the weight parameters, $w/(1+w)$, $1/(1+w)$ and -1 for regions L_{ab}, L_ε and L_δ respectively, where $w = 3$. Nederveen derives a marker value (MV) for each pixel position using:

$$MV = \frac{w}{1+w} I_{ab} + \frac{1}{1+w} I_\varepsilon - I_\delta \qquad (1)$$

where I_{ab}, I_ε and I_δ are the average pixel values in the central part

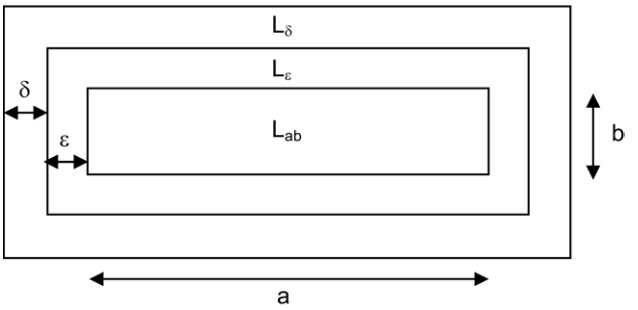

Fig. 2. Marker extraction kernel that consists of a central region L_{ab} and 2 borders L_ε and L_δ. Parameters a and b are the marker length and width found from the digitally reconstructed radiographs.

L_{ab} and the border area L_ε and L_δ of the MEK. Nederveen *et al.* 2002 (11) describe a method for calculating a weighting function which compares the second derivative of a function that mimics the shape of the marker images. Again because the markers are cylindrical the weighting function can be expected to change with the orientation of the marker. The weighting function therefore has to be derived from portal images of markers at each orientation or some "average" weighting function must be chosen to represent the marker at all orientations. Note that this weighting function cannot be obtained from the DRR as the pixel resolution of the DRR is often inadequate to describe the spatial variation of intensity at the marker edges. Nederveen *et al.* (11) note that the weights used for their MEK are comparable to the integer weights given in Nederveen *et al.* (6) and therefore these weights were used. Applying the weights recommended in Nederveen *et al.* (6) (w = 3) directly to the MEK produces the template shown in Figure 3A. The convolution of the image with the weighted MEK shown in Figure 3A produces a marker value (MV) which gives maximal response when the MEK is centered on a marker-like shape. In this way the MV is equivalent to the correlation coefficient. When we convolve the MEK with the search region of the image, we are effectively overlaying the center of MEK on each pixel of the search region and then calculating the MV value for this area under the MEK via convolution. By visiting each pixel in turn we generate an array of MV values the size of the search region. The higher the MV value the more similar that part of the search region is to the MEK. Therefore we say that the marker is found at the position of the pixel with the maximum MV value. To compare MV values from different images, the MV value is normalized by the average image intensity, this gives a marker value between 1 and 0, with maximum similarity being 1.

Buck *et al.* (8) propose an elliptical Mexican hat filter (MHF) for the detection of cylindrical markers based on the second derivative of the Gaussian function which has different widths for x and y directions and is fitted to:

$$-\left(\frac{d}{dx^2}+\frac{d}{dy^2}\right)f = \frac{1}{ab}\left(1-\left(\frac{x^2}{a^2}+\frac{y^2}{b^2}\right)\right)e^{-\left[\frac{x^2}{2a^2}+\frac{y^2}{2b^2}\right]} \qquad (2)$$

Marker templates were created using values of a and b that represent the dimensions of the marker projection in the x- and y-directions respectively; again values were acquired from the DRRs. An example of the MHF template ($a = 10$, $b = 4$) is shown in Fig. 3B. This shows the negative lobes characteristic of the

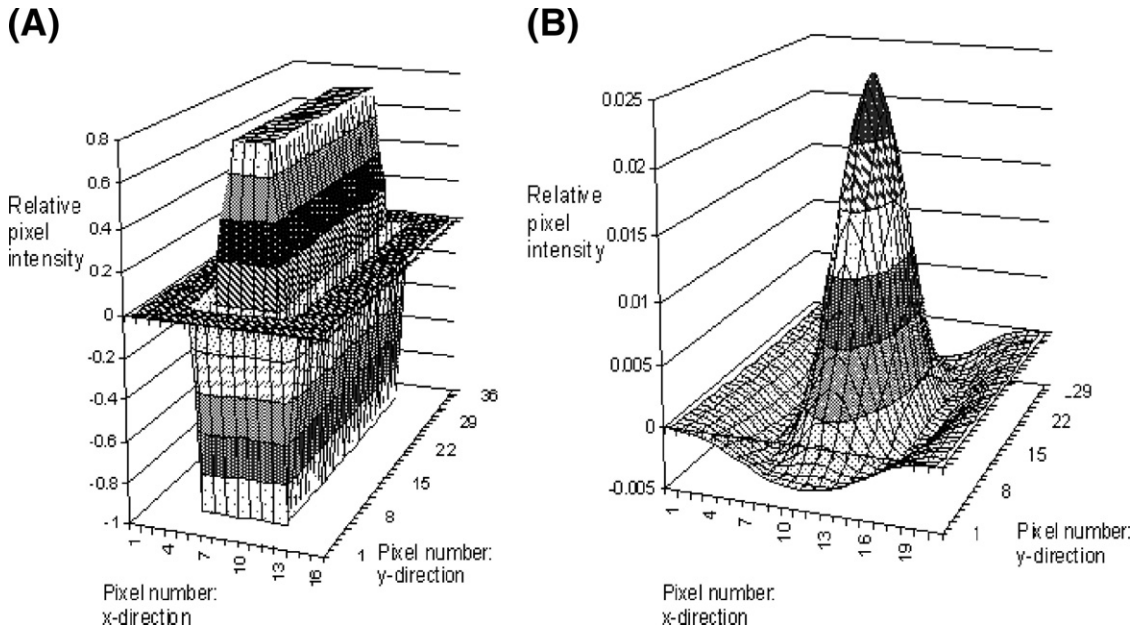

Fig. 3. Templates used to detect fiducial markers (A) Marker Extraction Kernel with weighting function applied described by Nederveen *et al.* (2000) and (B) Mexican Hat Filter used by Buck *et al.* (2003).

second derivative. The negative values in both of these templates make them more sensitive to objects that are the same size as the marker. Without these negative values uniform areas of high intensity will give greater values when convolved with the template.

Before convolution with the portal images, both MEK and MHF templates were rotated to match the orientation of the markers at the time of planning CT. Search areas of 64 × 64 pixels centered on predicted marker locations obtained using the DRR were defined. MEK and MHF marker templates were simply convolved with the search area and the pixel with the maximum intensity in the resultant image corresponds to the marker location. Because the markers are able to rotate within the patient, marker templates were rotated in steps of 5 degrees through +20 to −20 degrees from their original orientation before being applied. This strategy was used by Nederveen, who also used cylindrical markers. The greatest MV or highest intensity corresponds to the detected marker orientation. It should also be noted that this only takes into account possible in-plane rotations for each of these methods. Nederveen also only considers potential in-plane rotation of the marker between the time of planning and treatment. If the marker rotates out-of-plane we could expect to see a change in the length of the marker. However by taking into account possible out-of-plane rotations we would have to significantly increase the number of times we applied the templates, a number of out-of-plane rotations would have to be considered for each in-plane rotation. Also the template matching method is significantly more sensitive to in-plane rotations than the variation in length of the marker. Consequently, we do not expect this to change the detection efficiency greatly and have restricted all analysis to in-plane rotations.

Attenuation analysis (Aubin method). Aubin *et al.* (9) have presented an algorithm based on the identification of image intensity minima which represent regions of maximum attenuation. A complete description of the 7 steps followed to implement the algorithm is given by Pouliot *et al.* (12). The steps followed by Pouliot are now briefly summarized:

1. Definition of search area (as for template matching described above)
2. Image filtering to reduce noise using a 3 × 3 pixel averaging filter and contrast enhancement via the application of contrast limited histogram equalisation
3. Local minima positions are identified by centering a 5 × 5 pixel window on each part of the image; a pixel is considered to be a local minimum if it has the smallest value within the window.
4. A contrast image is formed (described in more detail below).
5. A point of interest (POI) lies at the coordinates of the minima obtained in step 3 in the contrast image. Weights are calculated for each POI by summing the pixel intensities in a 11 pixel diameter ring centered on the POI.
6. The inter-marker distances, x_1, x_2, y_1 and y_2, obtained from the DRR, as shown in Fig. 4A, are used in a "constellation analysis". Each POI in the contrast image is visited in turn. Assuming that the POI represents the central marker (shown in

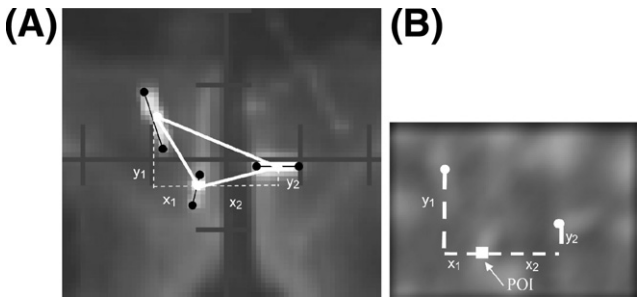

Fig. 4. (A) Inter-marker distances in terms of their x- and y-components (x_1, x_2, y_1 and y_2) are found by measuring the distance in pixels between the center of each marker in the digitally reconstructed radiographs. (B) A contrast image showing a point of interest (POI) and the 2 POIs associated with it found using the inter-marker distances.

Table 2. Percentage detection success rates for the four automatic marker detection methods compared in this study

	1MU		15MU	
	Anterior	Lateral	Anterior	Lateral (wedge)
MEK (Nederveen *et al.*)	75	37	93	58
MHF (Buck *et al.*)	72	35	90	59
Attenuation analysis	91	42	96	67
Cross correlation	99	83	100	99

Abbreviations: MEK = Marker Extraction Kernel; MHF = Mexican hat filter; MU = monitor units.

Fig. 4B) and using the distances x_1, x_2, y_1 and y_2 the 2 other POIs are identified as the POIs closest to the image co-ordinates given by the inter-marker distances. The weights for the 3 POIs are summed, the greatest combined weights gives the most probable marker positions.

7. Marker validation by neural network.

Because Aubin *et al.* describe an algorithm suitable for spherical markers changes to step 4 had to be made to optimize the method for cylindrical markers. In step 4, Aubin separately convolves unit ring and unit circle templates with the search area image and divides the resulting convolved circle image by the ring image to create a "contrast" image. This mimics the effect of the negative values in the templates employed by Buck and Nederveen, giving larger values where marker shapes are found. For this study, elliptical templates were employed in steps 4 and 5, the size, shape and orientation of the ellipses were varied according to the size and orientation of the marker projection in the DRR. An example of a contrast image is shown in Fig. 4B. The reader is referred to Pouliot, 2001 (12) for a complete description of the determination of the weights by Aubin. Step 7 described by Pouliot was used to validate the marker selection and categorise whether the marker detection was true or false, this stage was omitted from the analysis.

Localization accuracy. To assess detection success rate, marker positions found with each of the methods should be compared with actual marker positions. Actual marker positions were determined by manually identifying the 2 ends of the markers in the portal image and calculating the coordinates of the center of the marker. Marker positions were most difficult to identify in the lateral images. To assess the uncertainty in the actual position due to inter-observer and intra-observer error, 3 observers identified 3 markers in 2 patients (6 markers in total) in 28 lateral set-up images (14 images per patient). Each observer was asked to carry out the analysis 3 times. The actual marker location of the 6 markers was found by taking the average coordinates over all the data sets. Absolute differences between the actual marker location and those found by the observers were calculated. The standard deviation (S.D.) in the absolute differences for each of the 3 observers, intraobserver error, was found to be 1, 1.5 and 1.5 pixels. To assess inter-observer variation, the absolute difference between the actual marker location and the average marker location averaged over the 3 repeat measurements was calculated and the standard deviation of this data set was found to be 1.4 pixels.

To compare the performance of the automatic marker detection techniques, it was considered that the detection success rate should be defined as the fraction of the marker positions that can be found within ± 4 pixels or ± 1 mm tolerance of the actual marker position. Uncertainties on the actual position introduced by the manual identification were reduced by the identification of marker locations 3 times in 3 different sittings, reducing this error to approximately 0.5 pixels. Inter-observer error is therefore the most dominant source of error. To account for this error the tolerance on marker positions was increased by 2 times the intraobserver error ($2 \times 1.4 \approx 3$ pixels), and therefore, marker locations obtained by the techniques described above were considered to be correct if they were within ± 7 pixels or ± 1.75 mm (in both x and y directions) of the manually identified marker position.

RESULTS

Detection success rate

Table 2 compares the percentage detection success rates for the 4 automatic marker detection methods described above. Detections rates are given separately for anterior and lateral images for both set up (1MU) and treatment-time images (15 MU).

In addition, the data were analyzed to investigate the reasons for detection failure. Marker detection failures were placed into 3 categories: bony anatomy, wrong marker and miss. The bony anatomy category was assigned if the automatic detection method located another region of high X-ray attenuation, i.e., that associated with bony anatomy. Wrong marker was allocated when the method found a marker but not the specific marker it was searching for and the third category was allocated when the method found a position close to the marker and cannot be placed into the bony anatomy or wrong marker categories. The results of this analysis are given as the percentage of detection failures that fall into each category in Table 3.

Table 3. Percentage of marker detection failures. See main body of text for explanation of categories.

	Anterior			Lateral		
	Bony anatomy	Wrong marker	Miss	Bony anatomy	Wrong marker	Miss
MEK	5	60	35	27	27	46
MHF	8	71	21	20	38	42
Attenuation analysis	78	0	22	70	4	26
Cross correlation	0	0	100	54	2	44

Abbreviations as in Table 2.

Improving localization confidence

In the above analysis of maker detection success rate, a detection success is defined as a marker found by the automatic detection algorithm and is located within 1.75 mm of the actual marker location (manually identified) for AP and LAT images respectively. The confidence we have in the method to correctly identify the marker position will depend on this detection success rate. Therefore, if we have a 95% detection success rate, which can also be referred to as the sensitivity of the technique, we have 95% confidence in the method to detect the marker correctly. If, for example, for automated patient set-up we have a confidence of 50% in our automatic detection algorithm and therefore as an extra measure half of the marker positions found by the method were manually checked, it can be expected that half of the wrongly identified markers will be discovered. This would raise the overall average confidence for combined automatic detection and manual checking of marker positions to 75%. However, both the template matching method and the cross-correlation method not only find the position of the best match for a particular image but also provide a measure of the similarity of the image to the MEK and reference image via the MV and CC respectively. Therefore it can be postulated that we will detect a higher fraction of the wrongly identified markers if we check the markers that have low MVs or CCs. In this way, the CC and MV could act as a "flag" to identify potential wrong marker positions and in this way potentially reduce the level of manual intervention required. To test this hypothesis, we have recorded the MVs and CCs for each marker and found the average MV and CCs for those that have been successfully detected and those that have not. These are compared in Table 4.

DISCUSSION AND CONCLUSIONS

The results in Table 2 show that the detection success rates for all methods increase for images taken with a higher number of monitor units. This is expected because increased dose results in greater signal to noise ratio enabling fiducial markers to be visualized more easily. If we compare the detection success rates for all four methods it is evident that the two template matching methods give similar results which is also unsurprising as the templates share similar characteristics, i.e., their shape and negative lobes to pick out cylindrical shapes, and are used in the same manner. Both template matching methods produced poorer results compared to those presented in the literature (Nederveen: 90% for 1 mm diameter markers, Buck: 95% for 1.5 mm diameter markers) however, neither Nederveen nor Buck placed the markers inside the patient which may favorably change the imaging geometry or scatter conditions. Buck *et al.* also used greater diameter markers and a higher number of MUs which is a more likely explanation of their higher detection rates. In all cases the cross correlation method produces the highest detection success rates. Comparison of detection success rates published for attenuation analysis (Aubin, 80%) compared to those obtained in this study is difficult because of the greatly different image acquisition parameters. Detections rates for the cross correlation method are similar however Balter published results for only 2 patients.

Table 4. Average marker values and correlation coefficients for detected and non-detected markers

	1MU		15MU	
	Anterior	Lateral	Anterior	Lateral
Marker value (Detected)	0.25	0.01	0.29	0.15
Marker value (Not-detected)	0.26	0.09	0.28	0.16
Correlation coef. (Detected)	0.78	0.65	0.8	0.85
Correlation coef. (Not-detected)	0.69	0.68	*	*

* Anterior image detection success was 100% and lateral images detection success rate was 99% and therefore only 2 markers were not detected.

Analysis of the marker positions given by the 4 methods shows that for anterior images a large contribution to the overall marker detection failure rate for MEK and MHF is the fact that the method has found 1 marker in preference to another (Table 3). The number of marker failures is greater for lateral images, which can be explained by a comparison of the average inter-marker distance for the 2 views, which are 15.2 mm and 10.6 mm for ANT and LAT views respectively. This shows that on average the images of the markers are closer together in the lateral view and therefore more likely to fall within each other's search region. This is avoided in the attenuation analysis method where all 3 marker positions are considered at once using the inter-marker distances (Fig. 4) hence the detection efficiency is higher. For MEK and MHF methods, this error could be reduced by making the search area smaller however this could result in higher detection failures as the markers would then be more likely to move outside of the search area. Another option is to increase inter-marker distances at the time of insertion however this may not always be practicable and could not be relied upon. Alternatively, if two markers are found at the same position, one of the markers could be "removed" from the image after convolution and then a second search of convolved image could be made to find the pixel with the maximum pixel value. Clearly, this would require more time and from the analysis given in Table 3 even if this further step eliminated wrong marker failures it would raise the detection success rate for the MEK and MHF methods to approximately 75% for lateral portal (1MU) images which is not as high as the detection success rate for cross-correlation and still represents a significant failure rate. Detection failures for the attenuation analysis tend to occur due to the misidentification of regional minima using inter-marker distances where minima from bony anatomy are situated close to marker minima. The cross correlation method uses a reference image that may include more than one marker if they are in close proximity and thus includes information about the background to a specific marker helping to distinguish between markers. For lateral images errors are due to poor image contrast and the

fact that in many cases the bony anatomy obscures marker shape. This problem is more significant for template matching and attenuation analysis that rely on the likeness of a set marker shape.

The cross-correlation method relies upon the greatest level of a-priory knowledge, an image of the marker *in vivo*. Therefore this method requires manual intervention on the first day of radiotherapy treatment and cannot be considered to be fully automated. The requirement for intervention at the time of the first fraction is also discussed by Nederveen *et al.* (11) who discuss the need for a manual check of the accurate detection of markers at the time of the first fraction. This is to ensure that all 3 markers are present and are not obscured by bony anatomy. Considering this requirement there is no obvious disadvantage of the cross-correlation method.

The results presented in Table 4 show there is no significant difference between MVs or CCs for successfully and unsuccessfully detected markers. We had postulated that the MV and CC could be used as an indication of whether the marker detection was likely to be incorrect or correct. However, as the CC and MVs are similar for both correctly and incorrectly detected markers, from Table 4 we can see this hypothesis is wrong and these values show no correlation with incorrect or correct detection. This is partly due to the fact that a large proportion of the incorrectly identified marker positions are those in which the wrong marker has been found and therefore the similarity between the MEK and the image is high. Also, high noise in the lateral images and the overlaying bony anatomy means that the CC and MV values are low even when the marker position is correctly detected. To further investigate ways of improving the cross-correlation method in the future, we will examine how the peak value of CC compares with the rest of the values in the array of CCs, i.e., some value of signal-to-noise in the correlation space (the array of CC values) to investigate if this can be used as a "flag" for incorrect markers.

For 1MU lateral images, the highest detection success rate is obtained with the cross correlation method (83%). This is problematic, especially in view of the fact that the method will always supply an answer and we have no measure of the confidence with which a particular marker is identified. However, detection success rates of 99% can be achieved with an almost eightfold increase in dose. Clearly these doses are too high to be used for purely imaging purposes however with the inclusion of markers there is scope to use a fraction of the treatment dose by employing the same fields as the treatment. The same arguments apply for intrafraction imaging, an increase in image dose will enable high detection success rates to be achieved. In contrast however, for portal imaging to be used to monitor prostate position during treatment, images must be obtained at suitably regular intervals. For lateral treatment fields, the dose per field is on the order of 150–200 MU and therefore 15MU represents approximately 10% of the dose delivered. This means that potentially 10% of the dose could be delivered with the prostate outside of the treatment space before the error is detected. A trade off between detection success rate and the potential fraction of incorrectly delivered dose therefore exists. One of the major contributing factors to intrafraction prostate motion is the rectal peristalsis and, for this reason, it can vary in speed significantly (2). Nederveen *et al.* (11) used a sampling time interval of 0.4s and showed that this short time interval was important to be able to detect sharp and quick prostate motion. For the movie sequences in this study the time sampling interval is 2.28s. Further work is required to identify the minimum dose and therefore minimum sampling time interval required to obtain close to 100% detection success rate. In conclusion we have directly compared 4 methods for the automatic detection of fiducial markers that have been implanted into the prostate. This work has shown that a fully automated method of marker detection for the first treatment fraction is likely to be unachievable using these methods and that using cross-correlation is the best technique for automatic detection on subsequent radiotherapy treatment fractions.

REFERENCES

1. Keall PJ, Todor AD, Vedam SS, *et al.* On the use of EPID-based implanted marker tracking for 4D radiotherapy. *Med Phys* 2004;31:3492–3499.
2. Ghilezan MJ, Jaffray DA, Siewerdsen JH, *et al.* Prostate gland motion assessed with cine-magnetic resonance imaging (cine-MRI). *Int J Radiat Oncol Biol Phys* 2005;62:406–417.
3. Shimizu S, Shirato H, Kitmura K, *et al.* Use of an implanted marker and real-time tracking of the marker for the positioning of prostate and bladder cancers. *Int J Radiat Oncol Biol Phys* 2000;48:1591–1597.
4. Gonzalez RC, Woods RE. Digital image processing. New York: Wiley; 1978.
5. Balter J, Lam KL, Sandler HM, *et al.* Automated localisation of the prostate at the time of treatment using implanted radiopaque markers. *Int J Radiat Oncol Biol Phys* 1995;33: 1281–1286.
6. Nederveen AJ, Lagendijk JJW, Hofman P. Detection of fiducial gold markers for automatic on-line megavoltage position verification using a marker extraction kernel (MEK). *Int J Radiat Oncol Biol Phys* 2000;47:1453–1442.
7. Nederveen AJ, Lagendijk JJW, Hofman P. Feasibility of automatic marker detection with an a-Si flat-panel imager. *Phys Med Biol* 2001;46:1219–1230.
8. Buck D, Alber M, Nusslin F. Potential and limitations of the automatic detection of fiducial markers using an amorphous silicon flat-panel imager. *Phys Med Biol* 2003;48:763–764.
9. Aubin S, Beaulieu L, Pouliot S, *et al.* Robustness and precision of an automatic marker detection algorithm for online prostate daily targeting using a standard V-EPID. *Med Phys* 2003;30;7:1825–1833.
10. Bijhold J, Gilhuijs KG, van Herk M, Meertens H. Radiation field edge detection in portal images. *Phys Med Biol* 1991;36: 1705–1710.
11. Nederveen AJ, van der Heide UA, Dehnad H, *et al.* Measurements and clinical consequences of prostate motion during a radiotherapy fraction. *Int J Radiation Oncology Biol Phys* 2002;53:206–214.
12. Pouliot S, Zaccararin A, Laurendeau D, Pouliot J. Automatic detection of three radio-opaque markers for prostate targeting using EPID during external radiation therapy. *International conference on image processing (ICIP).* 2001:857–60.